Nano Energy xxx (xxxx) 105842

Contents lists available at ScienceDirect

Nano Energy

journal homepage: www.elsevier.com/locate/nanoen

Metal oxide-mediated differential chalcogen morphogenesis for Li-chalcogen battery application

Ayman A. AbdelHamid, Jian Liang Cheong, Jackie Y. Ying *

NanoBio Lab, Agency for Science, Technology and Research, 31 Biopolis Way, The Nanos, Republic of Singapore 138669

ARTICLE INFO

Keywords:
Chalcogens
Metal oxides
Sulfur
Selenium
Lithium batteries
Nanosheets

ABSTRACT

Chalcogens, especially sulfur and selenium, have wide-ranging applications, from pharmaceuticals to catalysis and energy storage. Size and morphology control are critical factors advancing the applications of sulfur and selenium. In this study, a new methodology for chalcogen nanostructure morphology control is established. The concept is based on harnessing the differential interaction of metal oxides with polysulfides and polyselenides to control the chalcogen nanostructure. Metal oxide substrates of varying compositions induce the formation of a wide range of multidimensional chalcogen morphologies, including nanoparticles and hollow nanospheres (0D), nanowires and nanocables (1D), uniform nanocoating (2D), and hollow-shell networks and multipods (3D). The chalcogen nanostructures are applied as Li-chalcogen battery cathodes. Battery testing shows direct structure-performance correlation, which favors smaller chalcogen size and shapes that allow closer contact with the substrate. Metal oxide-mediated chalcogen morphology control is a general strategy that can be applied to other fields for the advancement of chalcogen-based applications.

1. Introduction

Chalcogens, especially sulfur and selenium, have high potential for application in various fields, including pharmaceuticals, waste water treatment, agriculture, catalysis, sensors, photovoltaics, and energy storage [1–5]. Size reduction and morphology control are major drivers of their advanced applications [3,4,6–11]. One of the most promising applications of S and Se is Li-chalcogen batteries, owing to their high theoretical capacities of 1672 [12] and 678 mAh g^{1} [13], respectively. Nanostructural tailoring and shape control are very effective strategies for achieving high-performance Li-chalcogen battery [14–21].

Controlled synthesis of nanostructured S and Se has received considerable attention. S and Se nanoparticles have been synthesized by various approaches, including acid-mediated thiosulfate/polysulfide disproportionation [2,14,22–25], Se precursor reduction and stabilization [10,20,26–30], H_2S oxidation [15,31], chalcogen-amine chemistry [19,32], and physical methods [17,33]. Nano S and Se morphology control strategies are limited, with mostly 1D nanostructures reported [34–44]. New methodologies for chalcogen nanostructure control need to be established to further advance their applications.

Polysulfides (PS) and Polyselenides (PSe) have complex interactions with polar inorganic materials, such as metal oxides and sulfides. Polar inorganic materials bind PS and PSe via different routes, including polar-polar, Lewis acid-base and redox interactions, displaying distinct variation in affinity, binding mechanism and strength, and surface diffusion [45–54]. Metal oxides were found to bind PS with varying strength [46], and some oxides were capable of oxidizing PS [47]. Oxide acidity and surface diffusion were manipulated to tune PS binding properties [45,49]. Periodic laws predicting PS and PSe binding have been proposed [48,50]. Although differential interaction of PS and PSe with polar inorganic materials is a well-established principle, it has not been used in controlled chalcogen synthesis. We hypothesize that polar inorganic substrates can be used as mediators for differential chalcogen morphogenesis due to their differential interaction with PS and PSe.

Herein, a new concept for controlling the morphology of chalcogen nanostructures is established. Metal oxides were used as mediators that directed the chalcogen growth based on their differential interaction with PS and PSe. Metal oxide (MO) substrates with different compositions induced the formation of a wide variety of 0D, 1D, 2D and 3D S and Se nanostructures. Sulfur nanoparticles (0D), nanowires (1D) and hollow-shell networks (3D) were induced by FeO, NiO and CoO, respectively. Se hollow nanospheres (0D), nanocables (1D), uniform nanocoating (2D) and multipods (3D) were produced by CoO-N, Ni-NiO, CoO and NiO, respectively (Scheme 1). The Li-chalcogen battery

* Corresponding author.
E-mail address: jyying@nbl.a-star.edu.sg (J.Y. Ying).

https://doi.org/10.1016/j.nanoen.2021.105842
Received 4 October 2020; Received in revised form 22 January 2021; Accepted 28 January 2021

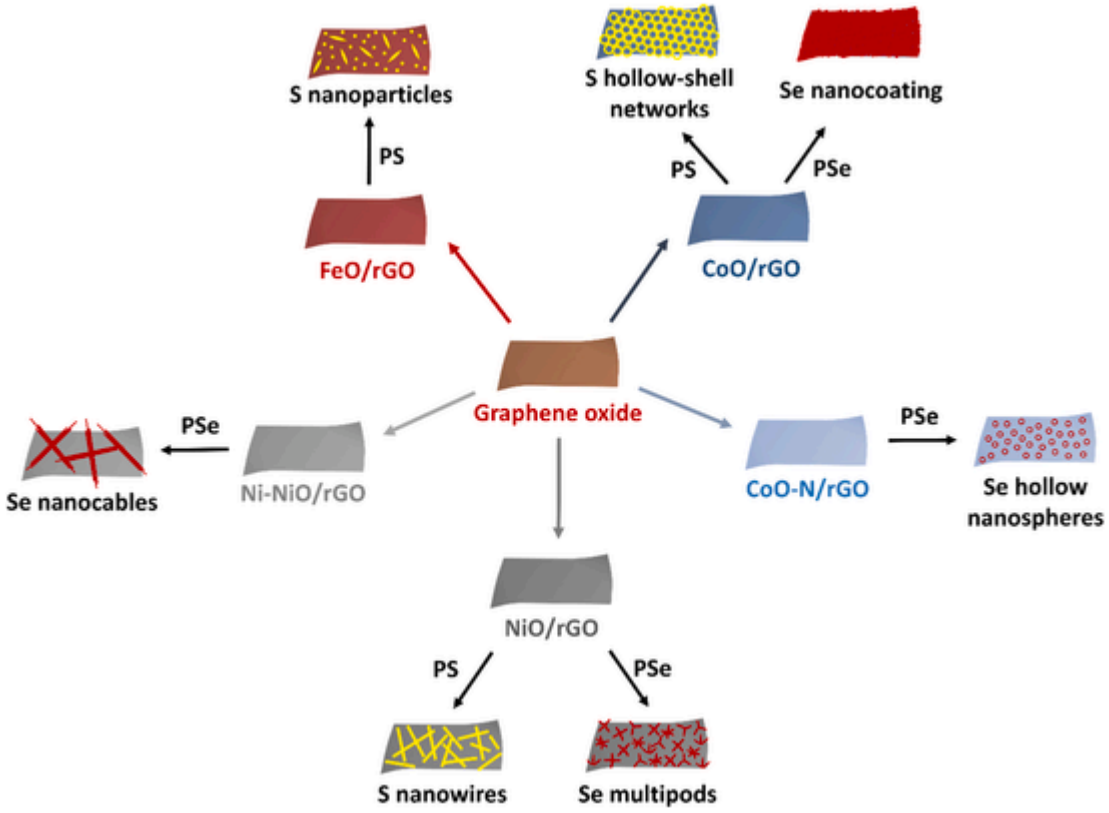

Scheme 1. Chalcogenide morphologies induced by different MO/rGO substrates.

performance of the synthesized nanostructures showed a distinct structure-performance correlation, whereby smaller S and Se nanostructures with shapes that allowed better contact with the substrate achieved better performance. These findings validated our hypothesis that the complex interactions of polar inorganic materials with PS and PSe could be harnessed for controlled S and Se morphogenesis, and demonstrated the importance of nanostructure control for advancing chalcogen-based applications.

2. Materials and methods

2.1. Synthesis of MO/rGO substrates

Metal oxide/rGO nanosheets were synthesized according to our previous report [55]. Briefly, metal oxide precursors (iron(III) acetylacetonate, cobalt(II) acetylacetonate and nickel(II) acetylacetonate) were dissolved (12.3 μmol mL^{-1}) in warm ethanol dispersions of graphene oxide (0.5 mg mL^{-1}). The dispersions were stirred overnight, and then washed with warm ethanol. The nanocomposites were dried at 60 °C and calcined at 300 °C in air. Nitridated and reduced substrates were calcined under NH_3 and Ar/H_2 (9:1) atmospheres at 400 °C and 350 °C, respectively.

2.2. Preparation of PS and PSe

PS and PSe were prepared by dissolving sulfur and selenium in ethylenediamine and hydrazine hydrate at concentrations of 0.2–2 M, forming alkylammonium PS and PSe, respectively, according to Eqs. (1)–(4) [32,56]. Mixture of ethylenediamine and hydrazine hydrate (volume ratio = 1:1) was used for the synthesis of NiO/rGO/Se and Ni-NiO/rGO/Se.

$$2(\text{R-NH}_2) + S_8 \rightarrow (\text{R-NH}_3^+)(\text{RNH-S}_8^{-}) \quad (1)$$

$$N_2H_4{\cdot}H_2O \leftrightarrow N_2H_5^+ + OH^- \quad (2)$$

$$4N_2H_5^+ + Se_8 + 20OH^- \rightarrow 4N_2 + 8Se^{2-} + 20H_2O \quad (3)$$

$$Se^{2-} + nSe \leftrightarrow Se_n^{2-} \quad (4)$$

2.3. Synthesis of chalcogen nanostructures

Chalcogen nanostructure synthesis was based on chalcogen-amine chemistry as previously reported [19,32], with modifications. MO/rGO substrates were dispersed at a concentration of 0.25 mg mL^{-1} in 55 mL of deionized water/ethanol mixture (volume ratio = 10:1). PS and PSe were added dropwise to the MO/rGO dispersions and stirred for 20 h. The nanocomposites were washed using deionized water and ethanol, and dried at 60 °C.

2.4. Characterization

Transmission/scanning transmission electron microscopy (TEM/STEM) and field emission scanning electron microscopy (FESEM) were conducted using FEI Tecnai F20 and JEOL JSM-7400 F, respectively, both fitted with energy dispersive X-ray spectroscopy (EDX) microanalyzer (OXFORD). Powder X-ray diffraction (XRD) and X-ray photoelectron spectroscopy (XPS) studies were performed using Bruker D8 ADVANCE and VG ESCALAB 220i-XL, respectively. Thermogravimetric analysis (TGA) and CHNS elemental analysis were obtained using TGA 55 (TA Instruments) and Thermo Scientific Flash*Smart* CHNS Elemental Analyzer, respectively. N_2 adsorption-desorption isotherms were attained using Micromeritics ASAP 2460.

2.5. Cathode preparation

Li-chalcogen battery cathodes were prepared by slurry coating or as self-standing electrodes. Slurry coating was carried out by mixing the nanocomposites with vapor-grown carbon fibers (VGCF) and poly (vinylidene fluoride) forming a slurry. The slurry was coated on carbon-coated Al foil, cut into 12.7 mm discs, and dried at 60 °C. Self-

standing electrodes were prepared by mixing the nanocomposites with reduced graphene oxide, VGCF and acetylene black using polytetrafluoroethylene, forming free-standing membranes. The membranes were cut into 12.7-mm discs and dried at 60 °C. S loading was 1.5–2 mg cm^2 and ~7 mg cm^2 for high-loading testing. Se loadings were 0.5, 1.2 and 1.7 mg cm^2. Specific capacity was based on the mass of active material. Electrodes with a low loading of 0.5 mg cm^2 were prepared by slurry coating, while those with loadings of 1.2–7 mg cm^2 were self-standing.

2.6. Electrochemical measurements

CR2032 coin cells were assembled in a glove box (Inert) under Ar atmosphere with O_2 and H_2O levels of < 1 ppm. The as-prepared cathodes were assembled against Li metal as counter and reference electrode, using Celgard 2325 as separator, and 1 M bis(trifluoromethane) sulfonimide lithium salt in a mixture of dimethoxyethane and 1,3-dioxolane containing 2 wt% $LiNO_3$ as electrolyte. CV and galvanostatic charge-discharge were conducted using AUTOLAB electrochemical workstation at 0.05 mV s^{-1} and LAND CT2001A battery cyclers at a voltage range of 1.6–2.8 V and 1/1.6–3 V for Li-S and Li-Se systems, respectively.

2.7. PS/PSe adsorption test

Li_2S_4 and Li_2Se_6 were synthesized in an Ar-filled glove box (Inert) by stirring stoichiometric amounts of sulfur and Li_2S, and selenium and Li, in 1,2-dimethoxyethane and 1,2-dimethoxyethane:1,3-dioxolane (1:1 v:v), respectively [57], overnight at 50 °C. 1.5 mL of Li_2S_4 (5 mM) or Li_2Se_6 (2.5 mM) solution was mixed with 10 mg of the test samples. The dispersions were then allowed to rest, and the supernatants were photographed and analyzed using ultraviolet-visible (UV-Vis) spectrophotometer (BioTek Instruments).

3. Results and discussion

3.1. MO/reduced graphene oxide (rGO) nanosheets

MO/rGO nanosheets were used as oxide substrates to induce differential chalcogen morphogenesis. A thin metal oxide layer was uniformly coated on rGO sheets, forming a high surface area 2D nanocomposite that would enhance exposure to PS and PSe, and allow chalcogen growth on its surface. The electronically conductive rGO sheets would improve and stabilize the electrochemical performance of the nanocomposites. MO/rGO nanosheets were synthesized as per our previous work [55]. Our MO/rGO nanosheet synthesis methodology could provide a platform for producing MO/rGO substrates with variable oxide composition and controlled 2D morphology. This enabled us to study the effect of metal oxide composition on the chalcogenide morphology and examine the impact of compositional modification on chalcogenide growth.

Iron, cobalt and nickel oxides were grown on rGO forming substrates that were used to study the effect of oxide composition on chalcogen nanostructure growth. The metal oxides were uniformly coated on the rGO sheets as shown by TEM and STEM images and EDX elemental maps (Figs. S1a—c, d—f). The metal oxide coatings were smooth and continuous without distinct particles. This could be explained by their amorphous nature as shown by XRD (Fig. S1j). The chemical compositions of the metal oxides were determined using XPS. Fe 2p core level spectrum showed Fe^{2+} to be the dominant oxidation state [58] (Fig. S1g). The $Fe^{2+/3+}$ ratio was estimated to be ~2.5, corresponding to a chemical composition of $FeO_{1.1}$. Co and Ni core level spectra indicated that the corresponding oxides existed as CoO and NiO [59,60], respectively (Fig. S1h,i). The three MO/rGO nanosheets were referred to as FeO/rGO, CoO/rGO and NiO/rGO. The metal oxide loadings in the nanocomposites were determined to be ~24 wt% using TGA (Fig. S1k). Brunauer–Emmett–Teller (BET) surface areas of FeO/rGO, CoO/rGO and NiO/rGO were measured to be ~47, ~30 and ~20 m^2 g^1, respectively, with a pore volume of 0.07, 0.05 and 0.04 cm^3 g^1 (Fig. S1l). The high surface area of FeO could be explained by the utilization of Fe(III) acetylacetonate as precursor, as compared to Co(II) and Ni (II) acetylacetonates in the cases of CoO and NiO, respectively. The 1.5× extra organic content in the FeO precursor might have resulted in controlled growth during thermal decomposition, and thus relatively higher surface area and porosity [61]. The relatively higher surface area of CoO, as compared to NiO could be due to the different effects of calcination on the oxides resulting in a denser coating in the case of NiO. NiO/rGO powder, which has the lowest surface area, appeared denser and harder to disperse as compared to the other nanocomposites.

In order to validate the effect of oxide compositional change on chalcogen nanostructure morphology, CoO/rGO and NiO/rGO nanosheets were modified to CoO-N/rGO and Ni-NiO/rGO nanosheets by nitridation and reduction under NH_3 and Ar/H_2 gases, respectively. The CoO-N and Ni-NiO nanoparticles were finely dispersed over the rGO sheets (Fig. S2a, S3a). Uniform distribution of Co, O and N was achieved for CoO-N/rGO (Fig. S2c), and uniform distribution of Ni and O was attained for Ni-NiO/rGO (Fig. S3c). CoO-N was amorphous (Fig. S2b), while Ni-NiO showed a distinct (111) and less intense (200) Ni XRD peaks at 44.5° and 51.9°, respectively (Fig. S3b). Nitrogen content in CoO-N/rGO was determined by CHNS elemental analysis to be 8.8 at%. N 1s peak appeared in the XPS survey spectrum of CoO-N/rGO (Fig. S2d), and its core level N1s spectrum showed the major peak at 398 eV, corresponding to Co—N bond [62] (Fig. S2e). The Co 2p XPS peaks at 780 eV and 795 eV confirmed Co—N bond formation [63] (Fig. S2f). Formation of metallic Ni in Ni-NiO/rGO was confirmed by the appearance of Ni^0 peaks in XPS Ni 2p core level spectrum at 853.5 eV and 871.9 eV [64] (Fig. S3d). The notable decrease in XPS peak intensity of oxygenated carbon groups in core level C 1s spectrum of Ni-NiO/rGO, as compared to that of NiO/rGO (Fig. S3e), was due to calcination under reducing environment.

3.2. MO-mediated differential chalcogen morphogenesis

Metal oxide substrates induced differential chalcogen morphogenesis upon interaction with PS and PSe. The role of rGO sheets supporting MO in controlling the chalcogen morphology was ruled out by testing rGO substrate as a control. rGO sheets only produced very small scattered S nanoparticles with negligible loading and amorphous Se aggregates when reacted with PS and PSe, respectively, under the same conditions (Fig. S4). FeO/rGO substrate induced the formation of 0D S nanoparticles (10 nm) and also spindle-like nanostructures (< 50 nm) as shown in Fig. 1a,d,g. CoO/rGO substrate promoted the formation of hollow S nanoshells (diameter: 100 nm, shell thickness: 10–15 nm) that fused together, forming 3D hollow-shell networks (Fig. 1b,e,h). NiO/rGO substrate produced S 1D nanowires with a diameter of 30–100 nm and length up to 1 μm (Fig. 1c,f,i). XRD patterns of the S nanostructures were indexed to orthorhombic S_8 (Fig. 1j). Analysis of (222) plane at 23.23° showed a broad peak, indicating nanometer crystallite size (Fig. 1k). A trend in peak width of nanoparticles > hollow-shell networks > nanowires was observed, corresponding to crystallite sizes of 46, 56 and 72 nm respectively, and was consistent with the TEM results. S loading was determined to be ~50 wt% using TGA (Fig. 1l).

CoO/rGO nanosheets induced the formation of 2D Se nanocoating on their surfaces (Fig. 2a—c). The nanocoating was composed of Se nanoparticles with no external Se structures observed. NiO/rGO drove the growth of 3D Se multipod microstructures comprising self-assembled Se nanoparticles (Fig. 2d—f). XRD patterns of the Se nanostructures were indexed to hexagonal Se with crystallite size of 50–60 nm (Fig. 2 g,h). Se loading in the nanocomposites was deter-

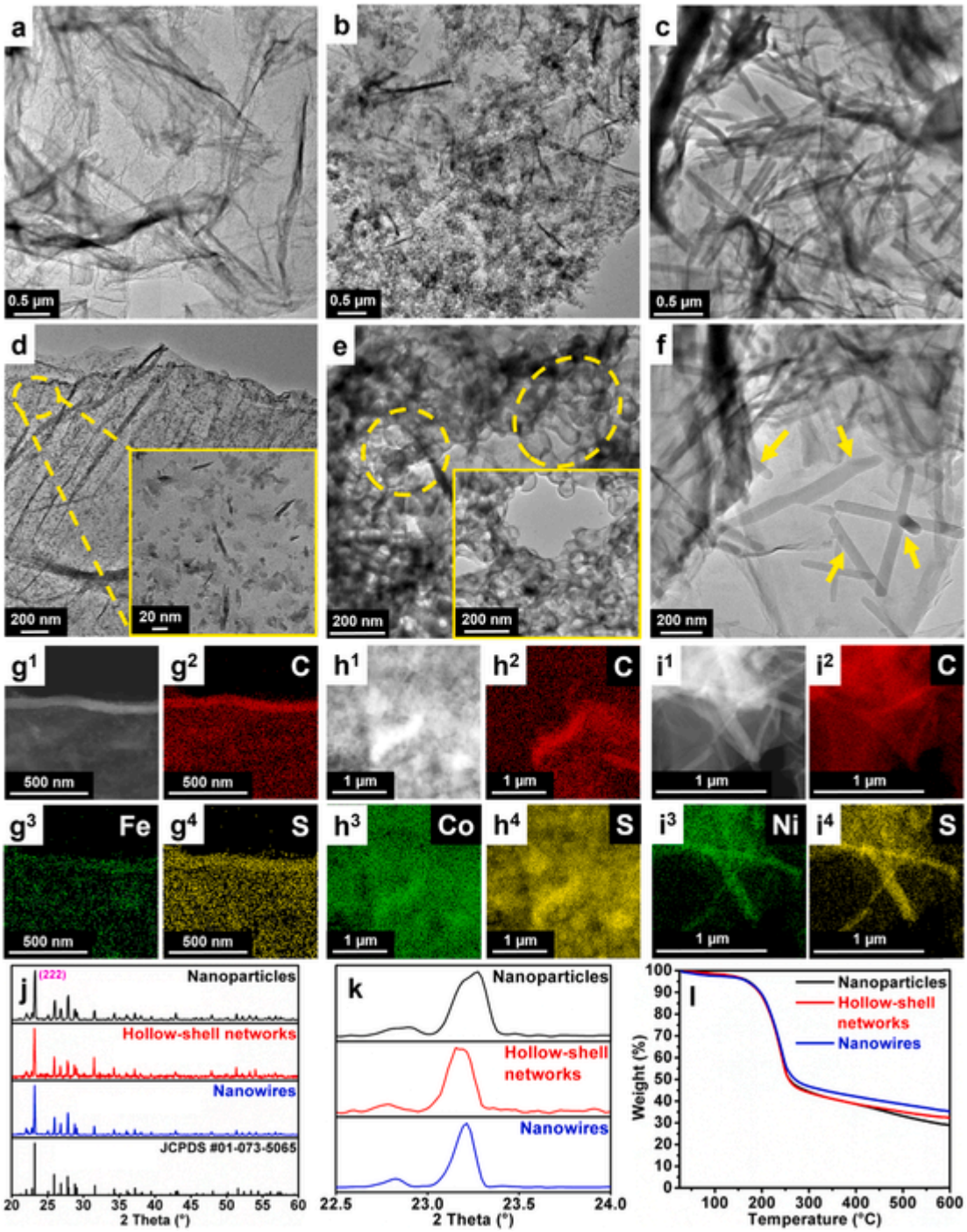

Fig. 1. (a—f) TEM and (g^1,h^1,i^1) STEM images, and (g^{2-4},h^{2-4},i^{2-4}) EDX elemental maps of (a,d,g) S nanoparticles on FeO/rGO, (b,e,h) S hollow-shell networks on CoO/rGO, and (c,f,i) S nanowires on NiO/rGO. (j) XRD patterns, (k) (222) XRD peak, and (l) TGA profiles of S nanoparticles on FeO/rGO, S hollow-shell networks on CoO/rGO, and S nanowires on NiO/rGO.

mined to be ~45 wt% (Fig. 2i). To the best of our knowledge, Se nanoparticle synthesis via PSe deposition from hydrazine solution has not been reported previously.

A time-dependent study was conducted to monitor the morphological evolution of the chalcogen nanostructures. Interestingly, it was found that the specific chalcogen nanostructure associated with each MO/rGO substrate was formed immediately after adding the PS/PSe precursors, as shown by the TEM images at 0 h of the synthesis (Fig. S5a—e). The density of S nanoparticles formed on FeO/rGO was very low at 0 h, but increased significantly at 1 h and 5 h (Fig. S5a). Scattered S hollow shells were formed on CoO/rGO at 0 h. They increased and started fusing with each other after 1 h, and finally formed interconnected networks after 5 h (Fig. S5b). S nanowires were formed on NiO/rGO at 0 h, and their size increased over time (Fig. S5c). Se nanocoating on CoO/rGO developed gradually; Se nanoparticles were not completely coating the substrate at 0 h, and a continuous coating only developed at 1 h and densified over time (Fig. S5d). Interestingly, evolution of Se multipods exhibited a distinct feature. Se nanowires were seen with the multipods at 0 h (Fig. S5e). These nanowires disappeared completely after 1 h and 5 h, which suggested that dissolution-precipitation process occurred over time. Interestingly, a slight modifi-

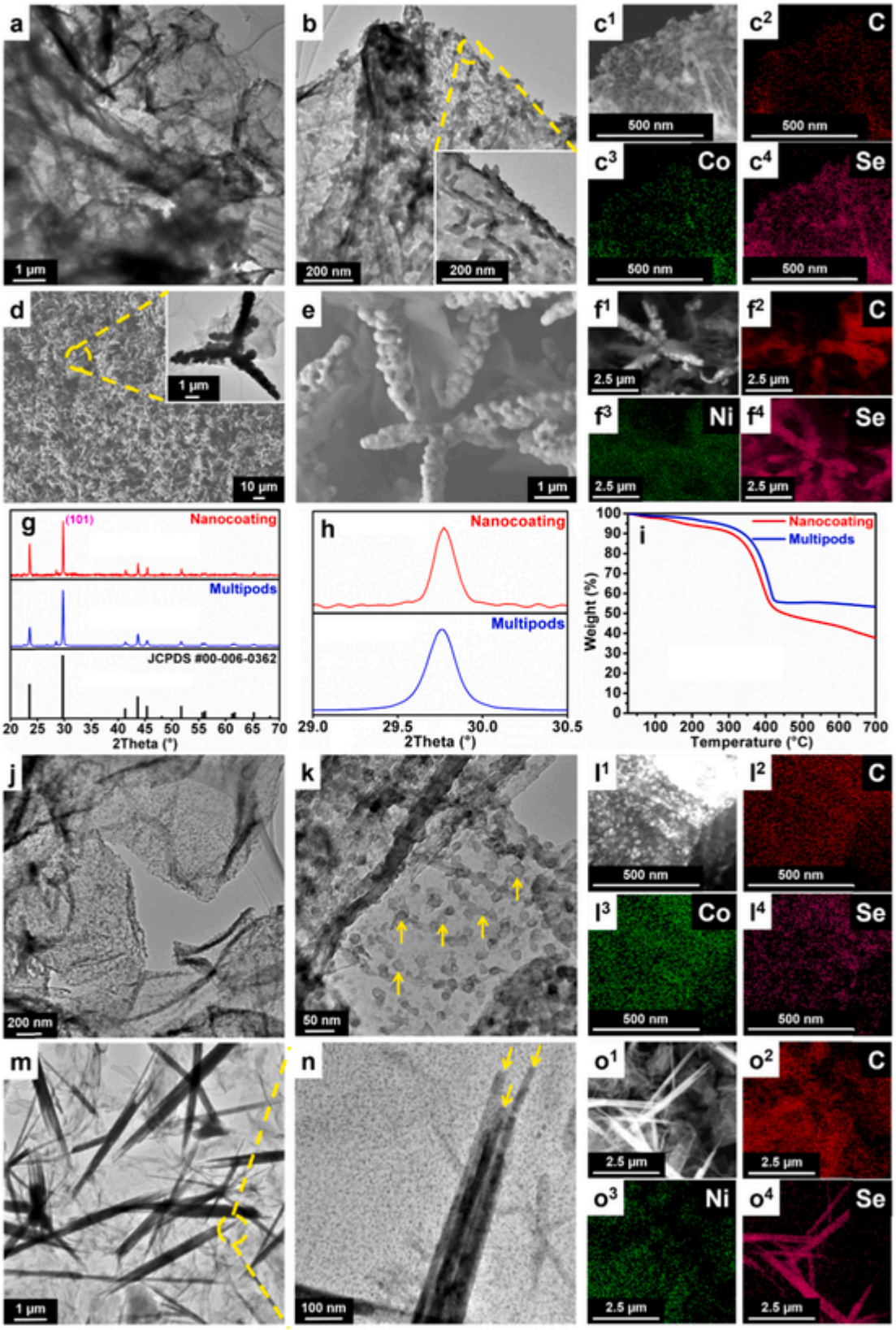

Fig. 2. (a,b,d (inset),j,k,m,n) TEM, (e,f[1]) FESEM and (c[1],l[1],o[1]) STEM images, and (c[2–4],f[2–4],l[2–4],o[2–4]) EDX elemental maps of (a—c) Se nanocoating on CoO/rGO, (d—f) Se multipods on NiO/rGO, (j—l) Se hollow nanospheres on CoO-N/rGO, and (m—o) Se nanocables on Ni-NiO/rGO. (g) XRD patterns, (h) (101) XRD peak and (i) TGA profiles of Se nanocoating on CoO/rGO and Se multipods on NiO/rGO.

cation of NiO/rGO substrate induced stable formation of Se bundled nanowires with no multipods observed, as shown later.

The mechanism of unique chalcogen nanostructure formation immediately after PS/PSe precursor addition on metal oxide substrates was intriguing. This could be explained by the complex nature of oxide-PS/PSe interactions, involving polar-polar, Lewis acid-base and redox reactions, in addition to variable surface diffusion [45–54]. These complex interactions might have changed the physicochemical properties of PS and PSe during their deposition, resulting in their different morphogenesis. Another possibility is the leaching of metal ions in the vicinity of the MO/rGO substrates, directing the growth of the chalcogen nanostructures on their surfaces. Metal ions have been reported as structure-directing agents of different nanostructures [65], with various mechanisms reported, such as stabilizing [66] or activating [67] certain facets, interfering with surfactant-facet interaction [68] and altering atomic diffusion [69]. An in-depth study is needed to investigate the different possibilities and determine the mode of metal oxide-PS/PSe interaction that results in the immediate formation of metal-specific unique chalcogen nanostructures.

To further validate our hypothesis of controlling chalcogen morphology by varying oxide composition, CoO/rGO and NiO/rGO were modified to test the effect of oxide substrate compositional change on Se morphology. CoO/rGO was nitridated while NiO/rGO was reduced, forming CoO-N/rGO and Ni-NiO/rGO nanosheets, respectively. Se deposition on the modified substrates produced different Se nanostructures, which proved that even a slight change in oxide composition could have a significant effect on the chalcogen morphology. CoO-N/rGO induced the formation of 20-nm 0D Se hollow nanospheres, uniformly dispersed over the CoO-N/rGO substrate (Fig. 2j—l), instead of the dense Se nanocoating formed on CoO/rGO. Ni-NiO/rGO promoted the formation of 1D nanocables comprising bundled nanowires of ~30 nm in diameter (Fig. 2 m—o), which were very different from the multipod microstructures that grew on NiO/rGO. Table 1 summarizes the morphologies and synthesis conditions of all chalcogen nanostructures reported in this study.

3.3. Li-chalcogen battery application

Li-chalcogen battery performance correlated well with the chalcogen nanostructure morphology. S nanoparticles and Se nanocoating showed good battery performance, which was comparable to recent reports (Table S1) [14–21], and significantly better than the other nanostructures (see Fig. S6 for cycling performance of MO/rGO substrates). S nanoparticles on FeO/rGO achieved ~1185, ~725, ~615, ~535 and ~410 mAh g^{-1} at 0.1. 0.2, 0.5, 1 and 2 C, respectively (Fig. 3a). Se nanocoating on CoO/rGO attained ~535, ~420, ~350, ~290 and ~220 mAh g^{-1} at 0.5, 1, 2, 5 and 10 C, respectively (Fig. 3e). S hollow-shell networks on CoO/rGO have good performance at low current densities, but their capacity decreased significantly as C-rate increased (Fig. 3a). S nanowires and Se multipods on NiO/rGO showed major capacity fading over cycling, resulting in poor stability (Fig. 3a,d). The performance trend correlated well with chalcogen structure, with the best performance obtained by S nanoparticles with the smallest size and uniform dispersion on FeO/rGO, which indicated very good S-substrate contact. Similarly, Se nanocoating on CoO/rGO that consisted of Se nanoparticles assembled uniformly on the substrate's surface forming a high-contact layer led to attractive performance. On the other hand, in spite of the small size, S hollow-shell networks did not show uniform dispersion or adequate contact with the CoO/rGO substrate due to the spatial limitation caused by the hollow particle morphology during S deposition. This resulted in lower battery performance, especially at high current densities. S nanowires extended over 1 μM in length, and Se multipods have a large-sized 3D microstructure, hence much of the deposited chalcogens were not in close contact with the NiO/rGO substrate, leading to high resistance and rapid capacity fading. These results demonstrated a clear correlation between the chalcogen nanostructure and its battery performance, whereby size and shape played critical roles in determining the electrochemical performance. Small chalcogen nanostructure dimensions and morphologies that allowed uniform dispersion on and good contact with the substrate led to greater access to Li^+ and enhanced conductivity, thus resulting in better electrochemical performance. This explanation was further supported by charge transfer resistance (R_{CT}) values of the nanocomposites, which increased in the order of S nanoparticles < S hollow-shell networks < S nanowires and Se nanocoating < Se multipods (Fig. S7a—c), and their charge-discharge polarization (ΔE) values, which also increased in the same order (Fig. S7d,e). This demonstrated the significance of size and morphology in improving the electrochemical properties of chalcogen nanostructures.

PS and PSe adsorption studies were conducted to investigate the role of MO/rGO substrate chemisorption in the different performance of the chalcogen nanocomposites (Figs. S8,9). PS/PSe chemisorption was displayed by all MO/rGO substrates, as evidenced by the enhanced PS/PSe adsorption vs. the higher surface area acetylene black (137 m^2/g), which agreed with previous reports [46,70,71]. FeO/rGO and CoO/rGO showed effective PS adsorption that was higher than that of NiO/rGO (Fig. S8). The lower PS adsorption capability of NiO/rGO could have contributed to its low battery performance. However, the comparable FeO/rGO and CoO/rGO PS adsorption capabilities indicated that the superior performance of S nanoparticles on FeO/rGO could only be explained by the morphological effect, whereby the fine size of S and its good contact with the substrate resulted in better electrochemical performance. Similarly, both CoO/rGO and NiO/rGO showed comparable PSe adsorption capabilities (Fig. S9), which indicated that their different battery performance would be better explained by their different morphologies, whereby the Se nanocoating on CoO/rGO was more favorable than the larger-sized Se multipods on NiO/rGO.

Long-term cycling of S nanoparticles on FeO/rGO and Se nanocoating on CoO/rGO was conducted at 0.5 C, achieving ~470 and ~305 mAh g^{-1} after 300 cycles, with Coulombic efficiencies of ≥ 97.4% and ~100%, respectively (Fig. 3b,d). Se nanocoating was further tested over 1000 cycles at 1 C, achieving ~190 mAh g^{-1} with a Coulombic efficiency of ~100% (Fig. 3f). The good stability of S nanoparticles and Se nanocoating could be explained by the small chalcogen nanoparticle size and good contact with the substrate, which stabilized the compos-

Table 1
Synthesis conditions and morphologies of chalcogen nanostructures.

Chalcogen morphology	Dimension (s) (D)	Chalcogen type	Chalcogen precursor	Precursor solvent	Substrate
Nanoparticles	0	S	PS	Ethylenediamine	FeO/rGO
Nanowires	1	S	PS	Ethylenediamine	NiO/rGO
Hollow-shell networks	3	S	PS	Ethylenediamine	CoO/rGO
Hollow nanospheres	0	Se	PSe	Hydrzaine hydrate	CoO-N/rGO
Nanocables	1	Se	PSe	Hydrzaine hydrate, ethylenediamine[a]	Ni-NiO/rGO
Nanocoating	2	Se	PSe	Hydrzaine hydrate	CoO/rGO
Multipods	3	Se	PSe	Hydrzaine hydrate, ethylenediamine[a]	NiO/rGO

[a] Volume ratio = 1:1.

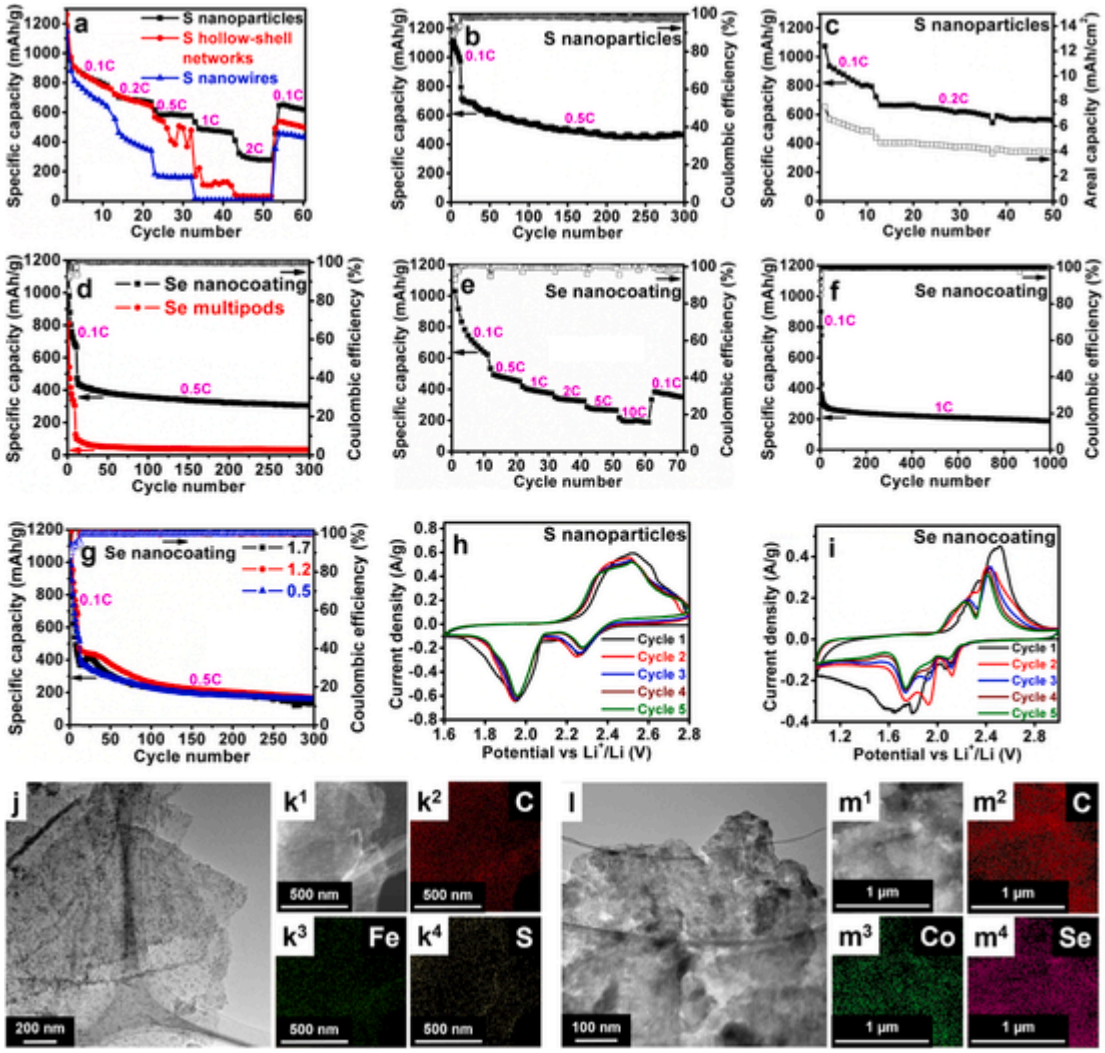

Fig. 3. (a) Rate capability of S nanoparticles on FeO/rGO, S hollow-shell networks on CoO/rGO, and S nanowires on NiO/rGO. (b) Cycling stability and (c) high-loading performance of S nanoparticles on FeO/rGO. (d) Cycling stability of Se nanocoating on CoO/rGO and Se multipods on NiO/rGO. (e) Rate capability, (f) long-cycling stability and (g) high voltage cutoff performance of Se nanocoating on CoO/rGO. (h,i) CV profiles and post-cycling (j,l) TEM and (k^1,m^1) STEM images, and (k^{2-4},m^{2-4}) EDX elemental maps of (h,j,k) S nanoparticles on FeO/rGO and (i,l,m) Se nanocoating on CoO/rGO.

ites even after prolonged cycling, as shown by post-cycling TEM and EDX analysis (Fig. 3j—m). Cyclic voltammetry (CV) profiles of S nanoparticles and Se nanocoating agreed with the literature [54,72]. The overlapping peaks after the first few cycles indicated electrochemical reversibility (Fig. 3h,i).

High loading of S nanoparticles on FeO/rGO was studied for more practical application. ~1074 mAh g^{-1} and ~723 mAh g^{-1}, corresponding to ~7.5 mAh cm^{-2} and ~5.1 mAh cm^{-2}, were achieved at 0.1 C and 0.2 C, respectively, which were higher than the conventional Li-ion battery standard of 4 mAh cm^{-2} [73], with good cycling stability demonstrated at 0.2 C (Fig. 3c). Performance of S nanoparticles on FeO/rGO was also demonstrated at lean electrolyte conditions, whereby the electrolyte-to-sulfur (E/S) ratio was reduced 3 times from 30 to 10. S nanoparticles on FeO/rGO showed a good performance at lean conditions, achieving ~800 mAh/g after 50 cycles at a sulfur loading of 3.9 mg cm^{-2} (Fig. S10). To attain a more practical Li-Se system, the lower voltage cutoff was raised from 1 V to 1.6 V, achieving ~170 mAh g^{-1} after 300 cycles at 0.5 C, which was maintained at increasing Se loadings (Fig. 3g). To achieve more practical performance, electrodes based on S nanoparticles on FeO/rGO and Se nanocoating on CoO/rGO need to be further developed by increasing chalcogen loading and minimizing inactive materials, which would enhance gravimetric and volumetric capacities.

The structure-performance correlation shown by the chalcogen nanoparticles demonstrated the significance of our oxide-mediated differential chalcogen morphogenesis strategy as a means to enhance Li-chalcogen battery performance, and its potential for advancing chalcogen-based applications in other fields.

4. Conclusion

In conclusion, a new concept of metal oxide-induced chalcogen differential morphogenesis was presented. Metal oxide substrates with different compositions promoted the formation of various chalcogen morphologies, including nanoparticles and hollow nanospheres (0D), nanowires and nanocables (1D), uniform nanocoating (2D), and hollow-shell networks and multipods (3D). Li-chalcogen battery performance correlated well with the chalcogen structure, whereby small size and shapes that allowed good contact with the substrate were found to be critical for high performance. This demonstrated the significance of controlling chalcogen morphology to enhance Li-chalcogen battery performance. Our oxide-mediated differential chalcogen morphogenesis strategy can be applied in various other fields in order to enhance chalcogens' performance and advance their applications.

CRediT authorship contribution statement

Ayman A. AbdelHamid: Conceptualization, Methodology, Investigation, Writing - original draft. **Jian Liang Cheong:** Methodology, Writing - review & editing. **Jackie Y. Ying:** Conceptualization, Writing - review & editing, Supervision.

Declaration of Competing Interest

The authors declare that they have no known competing interests that could have appeared to influence the work reported in this paper.

Acknowledgments

This work was funded by NBL (Biomedical Research Council, Agency for Science, Technology and Research, Singapore).

Appendix A. Supporting information

Supplementary data associated with this article can be found in the online version at doi:10.1016/j.nanoen.2021.105842.

References

[1] D.A. Boyd, Angew. Chem. Int. Ed., 55, 2016, pp. 15486–15502.
[2] R.G. Chaudhuri, S. Paria, Synthesis of sulfur nanoparticles in aqueous surfactant solutions, J. Colloid Interface Sci. 343 (2010) 439–446.
[3] Y. Lan, B. Deng, C. Kim, E.C. Thornton, H. Xu, Catalysis of elemental sulfur nanoparticles on chromium(VI) reduction by sulfide under anaerobic conditions, Environ. Sci. Technol. 39 (2005) 2087–2094.
[4] S. Thakur, G. Das, P.K. Raul, N. Karak, Green one-step approach to prepare sulfur/reduced graphene oxide nanohybrid for effective mercury ions removal, J. Phys. Chem. C 117 (2013) 7636–7642.
[5] S. Chaudhary, A. Umar, S.K. Mehta, Selenium nanomaterials: an overview of recent developments in synthesis, properties and potential applications, Prog. Mater. Sci. 83 (2016) 270–329.
[6] S. Shankar, R. Pangeni, J.W. Park, J.-W. Rhim, Preparation of sulfur nanoparticles and their antibacterial activity and cytotoxic effect, Mater. Sci. Eng.: C 92 (2018) 508–517.
[7] L.D. Geoffrion, T. Hesabizadeh, D. Medina-Cruz, M. Kusper, P. Taylor, A. Vernet-Crua, J. Chen, A. Ajo, T.J. Webster, G. Guisbiers, Naked selenium nanoparticles for antibacterial and anticancer treatments, ACS Omega 5 (2020) 2660–2669.
[8] W. Liu, X. Li, Y.-S. Wong, W. Zheng, Y. Zhang, W. Cao, T. Chen, Selenium nanoparticles as a carrier of 5-fluorouracil to achieve anticancer synergism, ACS Nano 6 (2012) 6578–6591.
[9] F. Gao, Q. Yuan, L. Gao, P. Cai, H. Zhu, R. Liu, Y. Wang, Y. Wei, G. Huang, J. Liang, X. Gao, Cytotoxicity and therapeutic effect of irinotecan combined with selenium nanoparticles, Biomaterials 35 (2014) 8854–8866.
[10] S. Nath, S.K. Ghosh, S. Panigahi, T. Thundat, T. Pal, Synthesis of selenium nanoparticle and its photocatalytic application for decolorization of methylene blue under UV irradiation, Langmuir 20 (2004) 7880–7883.
[11] H. Cheng, Z. Cao, Z. Chen, M. Zhao, M. Xie, Z. Lyu, Z. Zhu, M. Chi, Y. Xia, Catalytic system based on Sub-2 nm Pt particles and its extraordinary activity and durability for oxygen reduction, Nano Lett. 19 (2019) 4997–5002.
[12] Z. Zeng, X. Liu, Sulfur immobilization by “Chemical Anchor” to suppress the diffusion of polysulfides in lithium-sulfur batteries, Adv. Mater. Interfaces 5 (2018) 1701274.
[13] A. Eftekhari, The rise of lithium–selenium batteries, Sustain. Energy Fuels 1 (2017) 14–29.
[14] M.R. Kaiser, Z. Ma, X. Wang, F. Han, T. Gao, X. Fan, J.-Z. Wang, H.K. Liu, S. Dou, C. Wang, Reverse microemulsion synthesis of sulfur/graphene composite for lithium/sulfur batteries, ACS Nano 11 (2017) 9048–9056.
[15] D. Liu, C. Zhang, Z. Xu, L. Zhang, W. Lv, X. Zou, F. Kang, L. Zhi, H.-M. Cheng, Q.-H. Yang, H2S + SO2 produces water-dispersed sulfur nanoparticles for lithium-sulfur batteries, Nano Energy 41 (2017) 665–673.
[16] Y. Zhang, K. Li, J. Huang, Y. Wang, Y. Peng, H. Li, J. Wang, J. Zhao, Preparation of monodispersed sulfur nanoparticles-partly reduced graphene oxide-polydopamine composite for superior performance lithium-sulfur battery, Carbon 114 (2017) 8–14.
[17] Z. Ma, L. Tao, D. Liu, Z. Li, Y. Zhang, Z. Liu, H. Liu, R. Chen, J. Huo, S. Wang, Ultrafine nano-sulfur particles anchored on in situ exfoliated graphene for lithium–sulfur batteries, J. Mater. Chem. A 5 (2017) 9412–9417.
[18] Z.W. Lu, Y.H. Wang, Z. Dai, X.P. Li, C.Y. Zhang, G.Z. Sun, C.S. Gong, X.J. Pan, W. Lan, J.Y. Zhou, E.Q. Xie, One-pot sulfur-containing ion assisted microwave synthesis of reduced graphene oxide@nano-sulfur fibrous hybrids for high-performance lithium-sulfur batteries, Electrochim. Acta 325 (2019) 134920.
[19] X. Wang, Z. Zhang, Y. Qu, G. Wang, Y. Lai, J. Li, Solution-based synthesis of multi-walled carbon nanotube/selenium composites for high performance lithium–selenium battery, J. Power Sources 287 (2015) 247–252.
[20] X. Peng, L. Wang, X. Zhang, B. Gao, J. Fu, S. Xiao, K. Huo, P.K. Chu, Reduced graphene oxide encapsulated selenium nanoparticles for high-power lithium–selenium battery cathode, J. Power Sources 288 (2015) 214–220.
[21] S. Fan, Y. Zhang, S.-H. Li, T.-Y. Lan, J.-L. Xu, Hollow selenium encapsulated into 3D graphene hydrogels for lithium–selenium batteries with high rate performance and cycling stability, RSC Adv. 7 (2017) 21281–21286.
[22] R.G. Chaudhuri, S. Paria, Growth kinetics of sulfur nanoparticles in aqueous surfactant solutions, J. Colloid Interface Sci. 354 (2011) 563–569.
[23] S. Shankar, J.-W. Rhim, Preparation of sulfur nanoparticle-incorporated antimicrobial chitosan films, Food Hydrocoll. 82 (2018) 116–123.
[24] M. Soleimani, F. Aflatouni, A. Khani, A new and simple method for sulfur nanoparticles synthesis, Colloid J. 75 (2013) 112–116.
[25] Y. Guo, J. Zhao, S. Yang, K. Yu, Z. Wang, H. Zhang, Preparation and characterization of monoclinic sulfur nanoparticles by water-in-oil microemulsions technique, Powder Technol. 162 (2006) 83–86.
[26] S.-Y. Zhang, J. Zhang, H.-Y. Wang, H.-Y. Chen, Synthesis of selenium nanoparticles in the presence of polysaccharides, Mater. Lett. 58 (2004) 2590–2594.
[27] Y. Zhang, J. Wang, L. Zhang, Creation of highly stable selenium nanoparticles capped with hyperbranched polysaccharide in water, Langmuir 26 (2010) 17617–17623.
[28] Q. Li, T. Chen, F. Yang, J. Liu, W. Zheng, Facile and controllable one-step fabrication of selenium nanoparticles assisted by l-cysteine, Mater. Lett. 64 (2010) 614–617.
[29] M. Panahi-Kalamuei, M. Salavati-Niasari, S.M. Hosseinpour-Mashkani, Facile microwave synthesis, characterization, and solar cell application of selenium nanoparticles, J. Alloy. Compd. 617 (2014) 627–632.
[30] H. Kong, J. Yang, Y. Zhang, Y. Fang, K. Nishinari, G.O. Phillips, Synthesis and antioxidant properties of gum arabic-stabilized selenium nanoparticles, Int. J. Biol. Macromol. 65 (2014) 155–162.
[31] A.S. Deshpande, R.B. Khomane, B.K. Vaidya, R.M. Joshi, A.S. Harle, B.D. Kulkarni, Sulfur nanoparticles synthesis and characterization from H2S gas, using novel biodegradable iron chelates in W/O microemulsion, Nanoscale Res. Lett. 3 (2008) 221–229.
[32] C. Wang, H. Chen, W. Dong, J. Ge, W. Lu, X. Wu, L. Guo, L. Chen, Sulfur–amine chemistry-based synthesis of multi-walled carbon nanotube–sulfur composites for high performance Li–S batteries, Chem. Commun. 50 (2014) 1202–1204.
[33] M. Quintana, E. Haro-Poniatowski, J. Morales, N. Batina, Synthesis of selenium nanoparticles by pulsed laser ablation, Appl. Surf. Sci. 195 (2002) 175–186.
[34] P. Santiago, E. Carvajal, D. Mendoza, L. Rendon, Synthesis and structural characterization of sulfur nanowires, Microsc. Microanal. 12 (2006) 690–691.
[35] I. Bezverkhyy, P. Afanasiev, C. Marhic, M. Danot, Template-free solution synthesis of sulfur microtubules, Chem. Mater. 15 (2003) 2119–2121.
[36] X.-Y. Xie, L.-Y. Li, P.-S. Zheng, W.-J. Zheng, Y. Bai, T.-F. Cheng, J. Liu, Facile synthesis, spectral properties and formation mechanism of sulfur nanorods in PEG-200, Mater. Res. Bull. 47 (2012) 3665–3669.
[37] B. Gates, Y. Yin, Y. Xia, A solution-phase approach to the synthesis of uniform nanowires of crystalline selenium with lateral dimensions in the range of 10–30 nm, J. Am. Chem. Soc. 122 (2000) 12582–12583.
[38] B. Gates, B. Mayers, B. Cattle, Y. Xia, Synthesis and characterization of uniform nanowires of trigonal selenium, Adv. Funct. Mater. 12 (2002) 219–227.
[39] B.T. Mayers, K. Liu, D. Sunderland, Y. Xia, Sonochemical synthesis of trigonal selenium nanowires, Chem. Mater. 15 (2003) 3852–3858.
[40] D. Kundu, F. Krumeich, R. Nesper, Investigation of nano-fibrous selenium and its polypyrrole and graphene composite as cathode material for rechargeable Li-batteries, J. Power Sources 236 (2013) 112–117.
[41] U.K. Gautam, M. Nath, C.N.R. Rao, New strategies for the synthesis of t-selenium nanorods and nanowires, J. Mater. Chem. 13 (2003) 2845–2847.
[42] B. Cheng, E.T. Samulski, Rapid, high yield, solution-mediated transformation of polycrystalline selenium powder into single-crystal nanowiresElectronic supplementary information (ESI) available: histogram of diameter distribution of as-prepared single-crystalline trigonal selenium nanowires, Chem. Commun. (2003) 2024 ⟨http://www.rsc.org/suppdata/cc/b3/b303755j⟩.
[43] X. Zhou, P. Gao, S. Sun, D. Bao, Y. Wang, X. Li, T. Wu, Y. Chen, P. Yang, Amorphous, crystalline and crystalline/amorphous selenium nanowires and their sifferent (De)lithiation mechanisms, Chem. Mater. 27 (2015) 6730–6736.
[44] S. Xiong, B. Xi, W. Wang, C. Wang, L. Fei, H. Zhou, Y. Qian, The fabrication and characterization of single-crystalline selenium nanoneedles, Cryst. Growth Des. 6 (2006) 1711–1716.
[45] X. Wang, T. Gao, X. Fan, F. Han, Y. Wu, Z. Zhang, J. Li, C. Wang, Tailoring surface acidity of metal oxide for better polysulfide entrapment in Li-S batteries, Adv. Funct. Mater. 26 (2016) 7164–7169.
[46] Y. Zhong, K.R. Yang, W. Liu, P. He, V. Batista, H. Wang, Mechanistic insights into surface chemical interactions between lithium polysulfides and transition metal oxides, J. Phys. Chem. C 121 (2017) 14222–14227.

[47] X. Liang, C.Y. Kwok, F. Lodi-Marzano, Q. Pang, M. Cuisinier, H. Huang, C. J. Hart, D. Houtarde, K. Kaup, H. Sommer, T. Brezesinski, J. Janek, L.F. Nazar, Tuning transition metal oxide-sulfur interactions for long life lithium sulfur batteries: the "Goldilocks" principle, Adv. Energy Mater. 6 (2016) 1501636.
[48] X. Chen, H.-J. Peng, R. Zhang, T.-Z. Hou, J.-Q. Huang, B. Li, Q. Zhang, An analogous periodic law for strong anchoring of polysulfides on polar hosts in lithium sulfur batteries: S- or Li-binding on first-row transition-metal sulfides, ACS Energy Lett. 2 (2017) 795–801.
[49] X. Tao, J. Wang, C. Liu, H. Wang, H. Yao, G. Zheng, Z.W. Seh, Q. Cai, W. Li, G. Zhou, C. Zu, Y. Cui, Balancing surface adsorption and diffusion of lithium-polysulfides on nonconductive oxides for lithium–sulfur battery design, Nat. Commun. 7 (2016) 11203.
[50] D.S. Choi, M.S. Yeom, Y.-T. Kim, H. Kim, Y. Jung, Polyselenide anchoring using transition-metal disulfides for enhanced lithium–selenium batteries, Inorg. Chem. 57 (2018) 2149–2156.
[51] Z. Li, J. Zhang, B.Y. Guan, X.W. Lou, Mesoporous carbon@titanium nitride hollow spheres as an efficient SeS2 host for advanced Li-SeS2 batteries, Angew. Chem. Int. Ed. 56 (2017) 16003–16007.
[52] T. Chen, W. Kong, M. Fan, Z. Zhang, L. Wang, R. Chen, Y. Hu, J. Ma, Z. Jin, Chelation-assisted formation of multi-yolk–shell Co4N@carbon nanoboxes for self-discharge-suppressed high-performance Li–SeS2batteries, J. Mater. Chem. A 7 (2019) 20302–20309.
[53] Y. Zhang, Y. Guo, B. Wang, Y. Wei, P. Jing, H. Wu, Z. Dai, M. Wang, Y. Zhang, An integrated hybrid interlayer for polysulfides/selenides regulation toward advanced Li–SeS2 batteries, Carbon 161 (2020) 413–422.
[54] Z. Zhang, X. Yang, X. Wang, Q. Li, Z. Zhang, TiO2–Se composites as cathode material for rechargeable lithium–selenium batteries, Solid State Ion. 260 (2014) 101–106.
[55] A.A. AbdelHamid, Y. Yu, J. Yang, J.Y. Ying, Generalized synthesis of metal oxide nanosheets and their application as Li-ion battery anodes, Adv. Mater. 29 (2017) 1701427.
[56] S.S. K, B.K.S. Chandra, S.O. N, S. Dharam, Preliminary polarographic studies of sulfur and selenium solutions in hydrazine hydrate, BCSJ 64 (1991) 3662–3664.
[57] M. Wang, Y. Guo, B. Wang, H. Luo, X. Zhang, Q. Wang, Y. Zhang, H. Wu, H. Liu, S. Dou, An engineered self-supported electrocatalytic cathode and dendrite-free composite anode based on 3D double-carbon hosts for advanced Li–SeS2batteries, J. Mater. Chem. A 8 (2020) 2969–2983.
[58] P.M. Hallam, M. Gómez-Mingot, D.K. Kampouris, C.E. Banks, Facile synthetic fabrication of iron oxide particles and novel hydrogen superoxide supercapacitors, RSC Adv. 2 (2012) 6672–6679.
[59] A. Jiang, N. Nidamanuri, C. Zhang, Z. Li, Ionic-liquid-assisted one-step synthesis of CoO nanosheets as electrocatalysts for oxygen evolution reaction, ACS Omega 3 (2018) 10092–10098.
[60] G. George, S. Anandhan, Synthesis and characterisation of nickel oxide nanofibre webs with alcohol sensing characteristics, RSC Adv. 4 (2014) 62009–62020.
[61] L. Guo, H. Arafune, N. Teramae, Synthesis of mesoporous metal oxide by the thermal decomposition of oxalate precursor, Langmuir 29 (2013) 4404–4412.
[62] Y. Zhang, B. Ouyang, J. Xu, G. Jia, S. Chen, R.S. Rawat, H.J. Fan, Rapid synthesis of cobalt nitride nanowires: highly efficient and low-cost catalysts for oxygen evolution, Angew. Chem. Int. Ed. 55 (2016) 8670–8674.
[63] Y.-Z. Li, T.-T. Li, W. Chen, Y.-Y. Song, Co4N nanowires: noble-metal-free peroxidase mimetic with excellent salt- and temperature-resistant abilities, ACS Appl. Mater. Interfaces 9 (2017) 29881–29888.
[64] M. Chhetri, S. Sultan, C.N.R. Rao, Electrocatalytic hydrogen evolution reaction activity comparable to platinum exhibited by the Ni/Ni(OH)2/graphite electrode, Proc. Natl. Acad. Sci. U. S. A. 114 (2017) 8986–8990.
[65] A.K. Guria, N. Pradhan, Doped or not doped: ionic impurities for influencing the phase and growth of semiconductor nanocrystals, Chem. Mater. 28 (2016) 5224–5237.
[66] J. Liu, S. Wang, K. Cai, Y. Li, Z. Liu, L. Liu, Y. Han, H. Wang, H. Han, H. Chen, A new type of capping agent in nanoscience: metal cations, Small 15 (2019) 1900444.
[67] L. Chen, M. Sakamoto, M. Haruta, T. Nemoto, R. Sato, H. Kurata, T. Teranishi, Tin ion directed morphology evolution of copper sulfide nanoparticles and tuning of their plasmonic properties via phase conversion, Langmuir 32 (2016) 7582–7587.
[68] W. Li, R. Zamani, M. Ibáñez, D. Cadavid, A. Shavel, J.R. Morante, J. Arbiol, A. Cabot, Metal ions to control the morphology of semiconductor nanoparticles: copper selenide nanocubes, J. Am. Chem. Soc. 135 (2013) 4664–4667.
[69] G. Zhu, J. Liu, S. Li, Y. Zuo, D. Li, H. Han, Nickel-ion-oriented fabrication of spiny PtCu alloy octahedral nanoframes with enhanced electrocatalytic performance, ACS Appl. Energy Mater. 2 (2019) 2862–2869.
[70] F. Wu, T.P. Pollard, E. Zhao, Y. Xiao, M. Olguin, O. Borodin, G. Yushin, Layered LiTiO2for the protection of Li2S cathodes against dissolution: mechanisms of the remarkable performance boost, Energy Environ. Sci. 11 (2018) 807–817.
[71] X. Liao, Z. Li, Q. He, L. Xia, Y. Li, S. Zhu, M. Wang, H. Wang, X. Xu, L. Mai, Y. Zhao, Three-dimensional porous nitrogen-doped carbon nanosheet with embedded NixCo3–xS4 nanocrystals for advanced lithium–sulfur batteries, ACS Appl. Mater. Interfaces 12 (2020) 9181–9189.
[72] A.A. AbdelHamid, J.L. Cheong, J.Y. Ying, Li7La3Zr2O12 sheet-based framework for high-performance lithium–sulfur hybrid quasi-solid battery, Nano Energy 71 (2020) 104633.
[73] J.L. Cheong, A.A. AbdelHamid, J.Y. Ying, A high-performance slurry-coated polysulfide cathode for lithium–sulfur battery, Nano Energy 66 (2019) 104114.

Ayman A. AbdelHamid is a Research Scientist at NanoBio Lab, Singapore. He received his M.Sc. in Nanoscience and Technology from Nile University, Egypt in 2012, and his PhD in Materials Science and Engineering from Nanyang Technological University, Singapore in 2017. His research interests include development of nanomaterials and nanocomposites for energy storage applications.

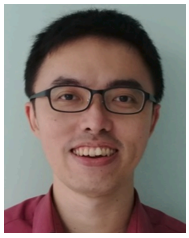

Jian Liang Cheong is a Senior Lab Officer at the NanoBio Lab, Singapore. He received his B.Sc. (Honours) in Chemistry from the National University of Singapore, Singapore in 2010. Currently, he is doing his PhD under the supervision of Prof. Jackie Ying. He is interested in developing practical and scalable systems for energy storage.

Jackie Y. Ying received her B.E. and PhD from The Cooper Union and Princeton University, respectively. She joined the faculty at Massachusetts Institute of Technology in 1992, where she was Professor of Chemical Engineering until 2005. She was the Founding Executive Director of the Institute of Bioengineering and Nanotechnology in Singapore from 2003 to 2018. Prof. Ying currently leads the NanoBio Lab as A*STAR Senior Fellow. For her research on nanostructured materials, Prof. Ying has been recognized with the American Ceramic Society Ross C. Purdy Award, David and Lucile Packard Fellowship, Office of Naval Research Young Investigator Award, National Science Foundation Young Investigator Award, Camille Dreyfus Teacher-Scholar Award, American Chemical Society Faculty Fellowship Award in Solid-State Chemistry, Technology Review's Inaugural TR100 Young Innovator Award, American Institute of Chemical Engineers (AIChE) Allan P. Colburn Award, International Union of Biochemistry and Molecular Biology Jubilee Medal, Materials Research Society Fellowship, Royal Society of Chemistry Fellowship, Crown Prince Grand Prize in the Brunei Creative, Innovative Product and Technological Advancement (CIPTA) Award, American Institute for Medical and Biological Engineering Fellowship, Academy of Sciences of Iran Medal of Honor, American Association for the Advancement of Science Fellowship, Academy of Sciences of Iran Medal of Honor, American Association for the Advancement of Science Fellowship, Islamic World Academy of Sciences-COMSTECH Ibrahim Memorial Award, Singapore National Academy of Science Fellowship, Islamic World Academy of Sciences Fellowship, U.S. National Academy of Inventors Fellowship, Clarivate Analytics Highly Cited Researcher, Turkish Academy of Sciences Academy Prize in Science and Engineering Sciences and Honorary Membership, and *Journal of Drug Targeting*'s Lifetime Achievement Award. Prof. Ying was elected a World Economic Forum Young Global Leader, and a member of the German National Academy of Sciences, Leopoldina. She was

named one of the “One Hundred Engineers of the Modern Era” by AIChE in its Centennial Celebration. She was the inaugural winner of the Mustafa Prize “Top Scientific Achievement Award” in 2015 for her research in bio-nanotechnology.